LARGE EDDY SIMULATION OF SUPERSONIC AXISYMMETRIC BASEFLOW

Christer Fureby
Dept. of Weapons and Protection, Weapons and Protection
The Swedish Defense Research Agency, FOI, S-172 90 Stockholm, Sweden

Marco Kupiainen
Dept. of Numerical Analysis and Computer Science, Royal Institute of Technology,
S-144 00 Stockholm, Sweden

ABSTRACT

Flows around missiles, rockets and projectiles often experience baseflow separation. This means that the pressure behind the base is considerably lower than the freestream pressure, causing base drag that often constitutes a large portion of the total drag. The present study is motivated by the fact that most methods used for reducing the drag often also reduce the aerodynamic stability of the vehicle. Semi-analytical methods and Reynolds Average Navier-Stokes (RANS) models often fail to provide accurate results for such flows, and therefore we use Large Eddy Simulations (LES) to investigate the flow physics of axisymmetric baseflow in a configuration for which experimental data is available for comparison. Good agreement with experimental data, with and without, base bleed is obtained for several LES models, suggesting that the details of the subgrid model are of less importance. The simulation data are also examined with the intention of increasing our knowledge of the underlying flow physics.

INTRODUCTION

Flows around missiles, rockets and projectiles often experience baseflow separation. This means that the pressure behind the base is lower than the freestream pressure, causing base drag that constitutes a large portion of the total drag, [1]. According to figure 1a, a recirculation region is formed behind the base. The size of this determines the flow turning angle coming off the base and the strength of the expansion waves. A small recirculation region leads to stronger expansion waves, lower base pressure and thus larger base drag. As the shear layer reattaches the flow is forced to turn along the axis of symmetry, causing the formation of a reattachment shock.

The drag cannot often be reduced without adversely affecting the aerodynamic stability of the vehicle. Recent attempts to reduce the drag have been directed towards reducing the base drag by means of boattails, [2-4], and base-bleed, [4-8]. By adding a boattail the recirculation is expanded through a non-zero local flow angle and a favourable pressure distribution on the tail. Base bleed, figure 1b, pushes the stagnation point further downstream. Thus, the importance of increasing the understanding of base flows lies in the possibility of controlling the near-wake flow interactions so that drag can be reduced without affecting vehicle stability, control and performance. However, with the exception of [4, 9-11], reliable experimental data in the base region is limited, thus presenting a problem in validating simulations.

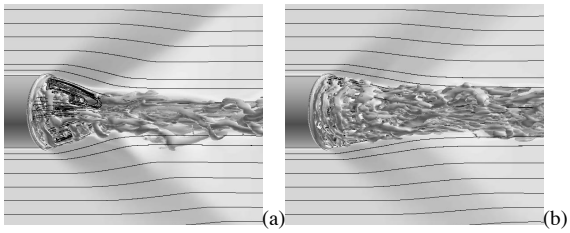

Figure 1. Axisymmetric baseflow in terms of Ma contours, streamlines and iso-surfaces of Q for (a) without base bleed (I=0) and (b) with base bleed (I=0.0113).

Early attempts to predict baseflows are summarized in Delery & Lacau, [12]. However, solving the underlying Navier-Stokes Equations (NSE) offers the ability to more realistically predict the details of the flow, and to remove many of the assumptions inherent in the simpler methods, and in addition more complex geometries require a more general approach. There are various techniques for the numerical prediction of turbulent flows governed by the NSE. These range from Reynolds Average Navier-Stokes (RANS) models, [13], via Large Eddy Simulation (LES) models, [14], Detatched Eddy Simulation (DES) models, [15] to Direct Numerical Simulation (DNS) models, [16]. Since large scales of separated flows are strongly dependent on the geometry RANS often fails to provide accurate results for such flows. Attempts to solve afterbody flows with RANS have been ongoing since the late 1970's. Putnam & Bissinger, [17], summarize these early attempts and conclude that the current methods were unable to accurately predict these flows.

Here, LES is used to examine the spatio-temporal behaviour of supersonic base-flow with and without mass-injection. In particular the experimental configuration used in [9-11] is chosen as a natural compactly characterised

test configuration. The aim is (i) to analyse the predictive capabilities of conventional LES and Monotone Integrated LES (MILES); (ii) to examine the sensibility of LES to the details of the subgrid models; (iii) to study the physics of supersonic base-flow from aerodynamic bodies of revolution, with and without mass-injection, and (iv) to generate a database of first and second order statistical moments of the velocity and pressure for use in calibrating and improving conventional RANS models.

THE CONVENTIONAL LES MODEL

In LES all variables f are split into resolved and subgrid components $f=\bar{f}+f'$, where $\bar{f}=G*f$ is the resolved part, $G=G(\mathbf{x},\Delta)$ the filter kernel and Δ the filter width. For variable density flows, Favré-filtering $\tilde{f}=\overline{\rho f}/\bar{\rho}$ is used so that $f=\tilde{f}+f''$. Convolving the NSE with G,

$$\begin{cases} \partial_t(\bar{\rho})+\nabla\cdot(\bar{\rho}\tilde{\mathbf{v}})=0, \\ \partial_t(\bar{\rho}\tilde{\mathbf{v}})+\nabla\cdot(\bar{\rho}\tilde{\mathbf{v}}\otimes\tilde{\mathbf{v}})=-\nabla\bar{p}+\nabla\cdot(\bar{\mathbf{S}}-\mathbf{B}), \\ \partial_t(\bar{\rho}\tilde{e})+\nabla\cdot(\bar{\rho}\tilde{\mathbf{v}}\tilde{e})=\nabla\cdot(\bar{\mathbf{h}}-\mathbf{b})+\bar{\mathbf{S}}\cdot\tilde{\mathbf{D}}+\bar{\rho}\varepsilon, \end{cases} \quad (1)$$

where ρ is the density, $\mathbf{v}$ the velocity, p the pressure, $\mathbf{S}=\eta\mathrm{tr}\mathbf{D}\mathbf{I}+2\mu\mathbf{D}_D$ the viscous stress, $\mathbf{B}=\bar{\rho}(\overline{\mathbf{v}\otimes\mathbf{v}}-\tilde{\mathbf{v}}\otimes\tilde{\mathbf{v}})$ the subgrid stress, $e=c_vT$ the internal energy (with T the temperature and c_V the specific heat), $\mathbf{h}=\kappa\nabla T$ the heat flux, $\mathbf{b}=\bar{\rho}(\overline{\mathbf{v}e}-\tilde{\mathbf{v}}\tilde{e})$ the subgrid flux, and $\bar{\rho}\varepsilon=\overline{\mathbf{S}\cdot\mathbf{D}}-\bar{\mathbf{S}}\cdot\tilde{\mathbf{D}}$ the subgrid dissipation. Here, $\mathbf{D}$ is the rate-of-strain tensor, η and μ the viscosities and κ the thermal conductivity.

Models for $\mathbf{B}$, $\mathbf{b}$ and ε are required to close (1) and to emulate the effects of the subgrid flow on the resolved flow. To this end we assume that,

$$\begin{cases} \mathbf{B}=\frac{2}{3}(\bar{\rho}k-\mu_k\nabla\cdot\tilde{\mathbf{v}})\mathbf{I}-2\mu_k\tilde{\mathbf{D}}_D, \\ \mathbf{b}=-\kappa_k\nabla\tilde{e}, \end{cases} \quad (2)$$

where k, μ_k and κ_k are the subgrid kinetic energy, eddy-viscosity and diffusivity, respectively. To close (2) we use the Smagorinsky (SMG) model, cf. [14, 18], $k=c_I\Delta^2\|\tilde{\mathbf{D}}\|^2$, $\nu_k=c_D\Delta^2\|\tilde{\mathbf{D}}\|$ and $\kappa_k=\mu_k/\mathrm{Pr}_t$, where $\mathrm{Pr}_t\approx0.7$ is the turbulent Pr-number. The model coefficients c_I and c_D are evaluated using either of the following approaches:

- an $|\mathbf{k}|^{-5/3}$ inertial sub-range behavior from which it follows that $c_D\approx0.02$ and $c_I\approx0.13$,
- scale-similarity between $\mathbf{B}$ and $\mathbf{L}=\bar{\rho}(\overline{\bar{\mathbf{v}}\otimes\bar{\mathbf{v}}}-\bar{\tilde{\mathbf{v}}}\otimes\bar{\tilde{\mathbf{v}}})$, [19-20], from which we have that $c_D=(\mathbf{L}_D\cdot\mathbf{S})/2(\mathbf{S}\cdot\mathbf{S})$ and $c_I=\bar{k}/(\bar{\Delta}^2\|\bar{\tilde{\mathbf{D}}}\|^2)$, where $\mathbf{S}=-\bar{\Delta}^2\|\bar{\tilde{\mathbf{D}}}\|\bar{\tilde{\mathbf{D}}}$.

Hereafter referred to as SMG and LDSMG, respectively. The self-similarity implies that both Δ and $\bar{\Delta}$ must lie in the inertial range, which also provides an estimate for the minimum grid resolution that can be used for a given Re-number. The denominators in the expressions for c_D and c_I are well defined at the test filter level and can be computed locally, which further implies that c_D and c_I can be evaluated locally without encountering any numerical problems as often is the case when using the dynamic model based on Germano's identity.

The LES equations are here discretized using an unstructured Finite Volume (FM) method, [21]. The discretization is based on Gauss theorem and a multi-step time-integration scheme, [21]. High-order reconstruction of convective fluxes and central differencing of inner derivatives gives second order accuracy in space, and Crank-Nicholson time-integration gives second order accuracy in time. Stability is enforced by using compact stenciles and by enforcing conservation of kinetic energy. The equations are usually solved sequentially, with iteration over the explicit source terms to obtain rapid convergence, with the stability requirement that Co<0.4.

THE MILES MODEL

As compared to conventional LES, where subgrid effects are represented by explicit models, cf. (2), MILES borrows particular features of some numerical schemes to construct implicit subgrid models by means of the truncation error, [22-23]. By incorporating a sharp velocity-gradient capturing capability operating at the smallest resolved scales, MILES seeks to emulate, the high-wavenumber end of the inertial subrange – characterized by thin filaments of intense vorticity embedded in a background of weak vorticity, [24-25]. MILES draws on the fact that finite difference, volume and element methods filter the NSE over cells – with typical dimension $|\mathbf{d}|$ – using a top-hat kernel. When founding MILES on concepts like the Flux Corrected Transport (FCT), [26], the functional reconstruction of the convective fluxes is done using a flux-limiting method combining a high-order flux-function with a low-order dispersion-free flux-function using a non-linear flux-limiter Γ. Moreover, the functional reconstruction of the viscous fluxes is typically done using linear interpolation. Similar approaches have been used by other groups, for a review see [27] and references therein. The modified equations provide the most suitable platform for comparing MILES and LES and following Fureby & Grinstein, [22-23] the implicit (or built-in) subgrid model is,

$$\begin{cases} \mathbf{B}=\rho(\mathbf{C}(\nabla\mathbf{v})^T+(\nabla\mathbf{v})\mathbf{C}^T+\chi^2(\nabla\mathbf{v})\mathbf{d}\otimes(\nabla\mathbf{v})\mathbf{d}), \\ \mathbf{b}=\rho(\mathbf{C}\nabla e+\chi^2(\nabla e\cdot\mathbf{d})(\nabla\mathbf{v})\mathbf{d}), \end{cases} \quad (3)$$

where $\mathbf{C}=\chi(\mathbf{v}\otimes\mathbf{d})$, $\chi=\frac{1}{2}(1-\Gamma)(\beta^- -\beta^+)$ with Γ being the flux limiter and $\beta=\beta(\Gamma)$. The built-in subgrid stress tensor can be split into two parts of which the former is a generalized eddy-viscosity term with $\mathbf{C}$ being the tensor-valued eddy-viscosity whilst the latter is of a form similar to the scale similarity part in a mixed model.

DESCRIPTION OF THE CASES

The configuration of this study is based on the experimental work by Dutton and co-workers, [9-11]. In the experiments, high-pressure air enters a stagnation chamber

and passes through a flow-conditioning module. The air is expanded to Ma≈2.46 in the test section using a converging diverging nozzle and exit by a conical diffuser and an exhaust duct to the surrounding air, see [28] for further details. The freestream velocity, pressure and temperature are u_∞=576 m/s, p_∞=515 kPa and T_∞=294 K, for the zero base-bleed case and u_∞=576 m/s, p_∞=471 kPa and T_∞=300 K, for the bleed case. The cases are characterized by the parameter $I=u_\infty \dot{m} A_b/\rho_\infty$, where $\dot{m}$ is the bleed mass flow rate, ρ_∞ the ambient density and A_b the base area. The afterbody in the experiments has a radius of r_b=31.75 mm, and for the base bleed cases it has a r_j=12.70 mm bleed orifice. The Reynolds number is $Re=45\cdot10^6$ m^{-1}, which amounts to a Re-number based on the freestream velocity u_∞ and the diameter D of the afterbody of $Re_D=2.86\cdot10^6$. For further details of the test conditions and and simulations carried out we refer to Table 1.

Table 1. Summary of simulations

Run	*I*	*Grid*	*SGS*
I	0	$0.7\cdot10^6$	MILES
II	0.0113	$0.7\cdot10^6$	MILES
III	0	$1.4\cdot10^6$	MILES
IV	0.0113	$1.4\cdot10^6$	MILES
V	0	$1.4\cdot10^6$	LDSMG
VI	0.0113	$1.4\cdot10^6$	LDSMG
VII	0.0226	$1.4\cdot10^6$	LDSMG

The computational domain consists of a circular cylinder with an outer radius of $6r_b$ and extending $8r_b$ upstream of the base-plane and $12r_b$ downstream of the base-plane, figure 2. Supersonic inflow conditions are imposed at the upstream boundary, and for the jet subsonic inflow conditions are imposed. Open boundary conditions, using a wave-transmissive condition, [29], are imposed at the downstream boundary, and in the cross-stream direction. Furthermore, no-slip adiabatic boundary conditions are imposed on the afterbody, and on the base-plane. The flow is initially set to the freestream conditions $(u_\infty, p_\infty, T_\infty)$ and is then advanced in time until all initial transients have disappeared, whereafter the statistical sampling is activated. This sampling is performed over about ten flow-through time. Simulations with different subgrid models, or bleed-rates, are restarted from previous simulations and require shorter time for initial transients to disappear.

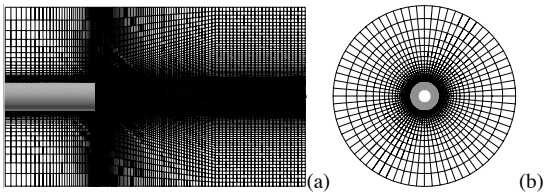

(a) (b)

Figure 2. Side views of the domain and the (coarse) mesh

Two grids are used to study the effects of the spatial resolution, figure 2. The average wall-normal direction, y^+, is 10 for the fine grid and 25 for the coarse grid, and the mesh is expanded radially using geometrical progression. In the streamwise direction geometrical progression is also used to expand the grid, but here we also take into consideration the expansion of the shear layers. The inflow velocity profile (at $x/r_b=-8.0$) is obtained by running a separate boundary layer code at the prevailing conditions resulting in a Blasus-type profile.

RESULTS

In figure 3 we show the base pressure coefficient C_P^b from simulations and experiments, [9]. C_P^b exhibits only small variations with r, except for a slight increase near the base corners, being in good overall agreement with the experimental data. From data, [9], it is clear that the mean base pressure initially increases with bleed-rate I, peaks around I=0.0148, and then decreases as I is increased further. This response is corroborated by simulations carried out at I=0, 0.0113 and 0.0226 showing this trend. C_P^b is however systematically overpredicted by 5%. A potential source of error may be the difference in approach boundary-layer thickness between the experiments and the simulations; a thick boundary-layer is thought to have a base pressure enhancing effect, similar to that of base-bleed. In the LES the approach boundary-layer is found to have a thickness of about δ≈2.6 mm and the associated friction velocity varies with I between u_τ=19.6 m/s and 22.5 m/s. In the experiments, [9-10], however, the approach boundary-layer thickness is δ≈3.2 mm so that the associated friction velocity is u_τ≈23.6 m/s.

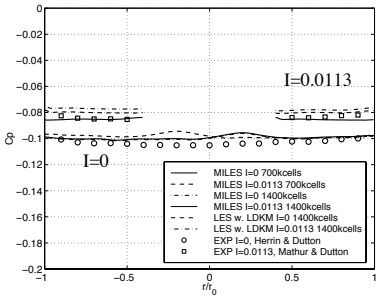

Figure 3. Distribution of the base pressure coefficient C_P^b across the base.

Figure 4 presents the axial velocity $\langle \tilde{v}_x \rangle / v_\infty$ along the centreline. For I=0 the predicted peak reverse velocity ($0.32u_\infty$ at x/r_b≈1.45) is in good agreement with the data ($0.34u_\infty$ at x/r_b=1.52) independently of grid and subgrid models. The rear stagnation point at x/r_b=2.45 is slightly shifted upstream when compared with the data for which x/r_b=2.65, [9]. For I=0.0148 the location of the rear stagnation point is x/r_b≈3.10 which is in good agreement with the data of x/r_b≈3.20. Hence, the observed downstream shift of the forward stagnation point with increasing bleed rate has the effect of decreasing the size of the recirculation region. The predicted peak reverse velocity is in close agreement with the experimental value of $-0.05u_\infty$. The position of the anticipated peak reverse velocity occurs

progressively downstream, its magnitude diminishing with increasing bleed rate I in the same manner as found in the experiments. Simulations of the highest bleed rate (I= 0.0226) case show no reverse flow, suggesting penetration of the bleed jet into the wake region.

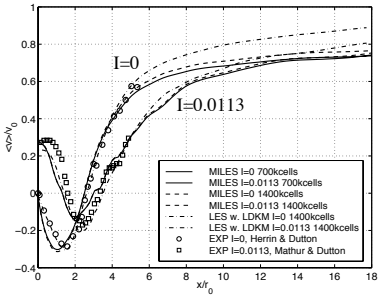

Figure 4. Comparison of $\langle \tilde{v}_x \rangle / v_\infty$ along the centerline for different values of I.

Contour plots of the mean axial and radial velocity components, $\langle \tilde{v} \rangle_x$ and $\langle \tilde{v} \rangle_r$ respectively, at the centerplane for I=0 and 0.0113 are presented in figure 5. The initial portion of the free shear layer is characterised by very high gradients of $\langle \tilde{v} \rangle_x$, and is in good qualitative agreement with the experimental data, [9], for I=0. The spreading of the axial velocity gradients is indicative of the development of the shear layer prior to reattachment, and also of the further wake evolution. Furthermore, the distribution of $\langle \tilde{v} \rangle_x$ in the free shear layer downstream of the base appears to be separated in an inner region and an outer region, of which the former appears to diverge more rapidly towards the centreline. The inner region finally overtakes the outer region and consumes most of the total shear layer width. These findings are in good qualitative accordance with the experimental data, [9-10]. The shape of the mean-velocity defect, and the associated recovery of $\langle \tilde{v} \rangle_x$ downstream of reattachment is dependent of I; along the centerline, the flow re-accelerates to sonic speed at $x/r_b \approx 4.8$ and 5.8, for I=0 and 0.0113, respectively. The $\langle \tilde{v} \rangle_r$ component is smaller than the $\langle \tilde{v} \rangle_x$ component, emphasizing the anisotropy in the near-wake. The high radial velocity gradient at the base corner marks the turning of the flow through the expansion fan, whilst the radial velocity gradient further downstream, occurring at the recompression region, marks the start of the trailing wake. As the outer flow approaches the axis of symmetry, the magnitude of $\langle \tilde{v} \rangle_r$ continues to increase due to the axisymmetric effect, to a peak value of about $0.24u_\infty$ for I=0 at approximately $2r_0$ downstream, and $0.29u_\infty$ for I= 0.0113 at around $3r_0$ downstream. The value of I clearly affects the strength of the recompression waves: for I=0 a strong recompression is observed in the simulations, whilst at higher values of I this weakens to expire at I=0.0226. Furthermore, the mean tangential velocity $\langle \tilde{v} \rangle_t$ component is negligible in comparison with $\langle \tilde{v} \rangle_r$ for all cases, however, it was observed to be larger when I≠0 and in particular for I=0.0226.

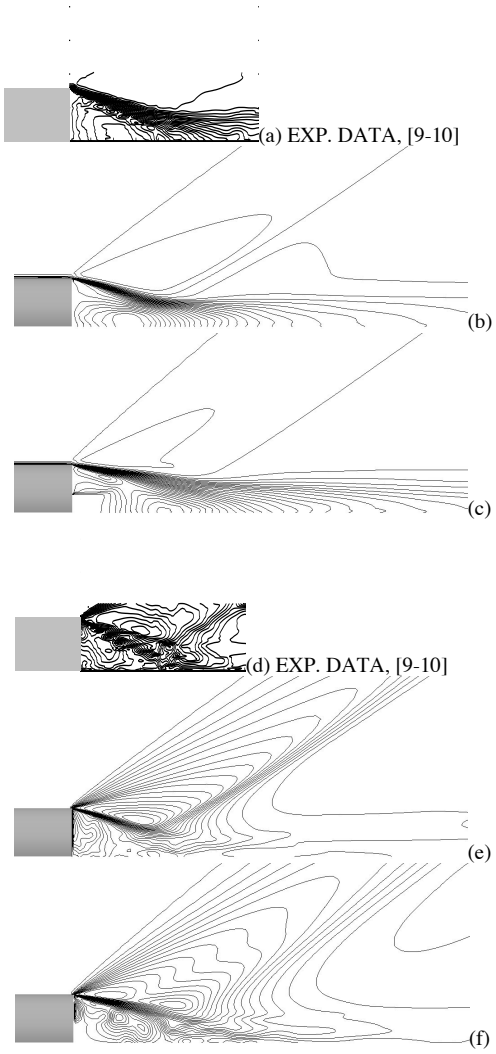

Figure 5. Distribution of the mean axial $\langle \tilde{v} \rangle_x$ (panels (a) (b) and (c)) and radial $\langle \tilde{v} \rangle_r$ (panels (d), (e) and (f)) velocity components at the centerplane for I=0 (panels (a), (b), (d) and (e)) and I=0.0113 (panels (c) and (f)).

Figure 6 shows composit plots for (a) I=0 and (b) I=0.0113 in terms of: Ma and ρ together with vortex cores in the upper panel, iso-surfaces of $Q = -\frac{1}{2}(\|\mathbf{D}\|^2 - \|\mathbf{W}\|^2)$ in the lower left panel, and endviews of ρ in the lower right panel. The flows are strongly three-dimensional and unsteady, having the additional effects of weakening the corner expansion and the downstream recompression. At the base corners, the expansion fans can be recognized by the increase in Ma followed by the gradual recompression in the freestream flow associated with a decrease in Ma. At low bleed rates, near the base, the flow is generally reversed virtually out to the corner, however, at higher bleed rates the flow only becomes reversed in the annular region around the bleed jet and downstream of the bleed jet, depending on the bleed rate. The free annular shear layer is turbulent and viscous, forming at the base corner and developing downstream to reattachment, whereupon it forms the far wake. The pressure gradient and the shear stress gradients in the shear layer are reduced as the shear layer

matures when turbulent mixing develops, entraining ambient fluid from the freestream into the wake. Base bleed seems to narrow the annular shear layer and move it further from the line of symmetry. The base bleed seems to increase the mixing near the corners, leading to reduction of shear stresses, but by directing most of the injectant into the recirculation region the downstream mixing seems not to be fully developed.

The vorticity distribution is extremly complicated and strongly dependent on I; for I=0 the vorticity is dominated by $\tilde{\omega}_x=(\nabla\times\tilde{\mathbf{v}})$ produced in the annular shear layer downstream of the base corner and in the region of mean reattachment. These axial vortices are unstable and exhibit a shedding-like behaviour. For I≠0 the annular Kelvin-Helmholtz instability, along the jet border, yields high intensity vortex structures mainly consisting of axisymmetric rings enclosing a region of intense axial vorticity. The axisymmetric vortex rings are short-lived and therefore only present in the near wake region and may occasionally alternate with helicoidal vortices. In the region of reattachment, large coherent structures, having a characteristic size of about $r_b/10$ – considerably larger than the mesh resolution Δ, are found in simulations and experiments, [11]. In the developing wake the endviews suggest that the coherent structures seem to have a preferred orientation of approximately ±45° from the principal axis that coincides with experimental data. Considering the end-view images it seems that the development and evolution of the large coherent structures is a realistic prediction based on the filtered NSE. For I≠0 the development of the flow in the reverse and redevelopment regions are different as may be seen in figure 6. In the shear layer the bleed jet dominates the flow field, close to the mean reattachment, however, the differences are less apparent, whilst further downstream, in the developing wake differences emerge as a result of the different flow, governed by the interactions of the free shear layers, the bleed jet and the expansion and recompression waves.

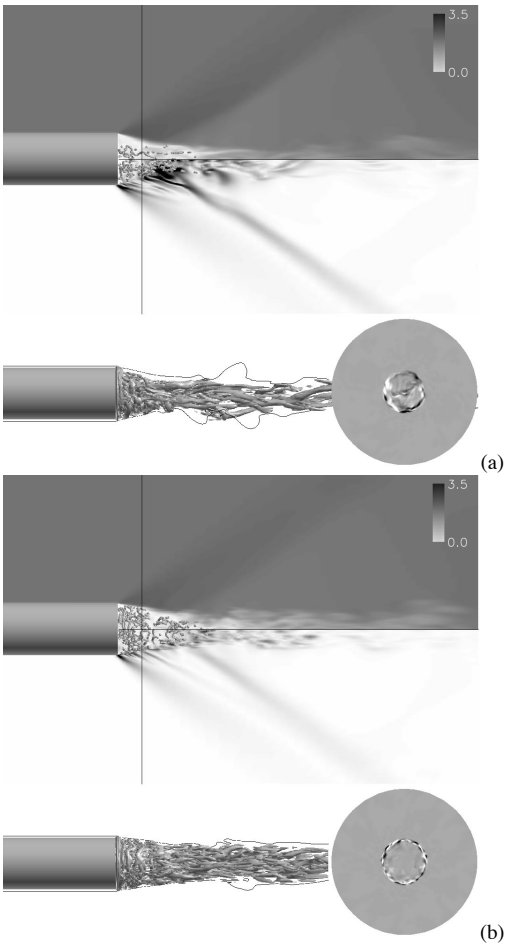

Figure 6. Ma and ρ contours together with vortex cores in the upper panel, iso-surfaces of Q in the lower left panel, and endviews of ρ in the lower right panel.

CONCLUDING REMARKS

In this study LES was used to examine the behaviour of axisymmetric supersonic base flow with and without base bleed. In order to investigate the influence of the subgrid model and the spatial resolution simulations for a zero base bleed case (I=0) were carried out using two different LES models, MILES and LDSMG on two grids. Good qualitative and quantitative agreement for both first and second order statistical moments between predictions and experiments can be observed. This suggests that the resolvable flow is fairly independent of the details of the subgrid model as observed elsewhere. Inproved agreement is obtained on the finer grid, on which more flow detailes are apparent. Additional sources of error (e.g. the discretization, the size of the computational domain and the far-field boundary conditions) will be examined in a forthcomming study. The influence of mass injection or base bleed on the near wake flowfield and on the pressure distribution on the base is investigated next. Again, good quantitative and reasonable qualitative agreement with experimental results for the first and second order statistical moments are found. In particular, the trends associated with altering the value of the mass injection I, are well reproduced by the simulations. Good agreement between predicted and measured pressure distributions, showing almost uniform radial mean pressure profiles across the base are observed. Furthermore, the mean base pressure increases with increasing base bleed I to attain a peak value at about I=0.0148, to then decrease with further increase in I. By analyzing the axial and radial velocity distributions at the centreplane it can be seen that an increase in bleed rate is accompanied by the decreasing size and intensity of the recirculation region (due to the downstream shift of the forward stagnation point) and a posterior reduction in the peak axial and radial rms-velocity fluctuations at the forward stagnation point. Injection increases the base pressure and therefore reduces the mean base drag. Maximum base pressure occurs when freestream flow turning is minimised. Thus, peak base pressures are reached when the entrainment of freestream air into the wake is minimised.

ACKNOWLEDGEMENT

The authors greatfully acknowledge the financial support of SAAB Bofors Dynamics (with J. Ekeroot serving as contract monitor). The authors thank C. Dutton for providing data and helpful information from his experimental studies and J. Forsythe for valuable discusions. These computations were preformed with an earlier research version of the FOAM™ code, see http://www.nabla.co.uk.

REFERENCES

[1] Rollstin L.; 1987, "Measurement of Inflight Base Pressure on an Artillery-Fired Projectile", AIAA Paper No. 87-2427.

[2] Addy A.L. & White R.A.; 1973, "Optimization of Drag Minimums Including Effects of Flow Separation" ASME Transactions: Journal of Engineering for Industry, **96**, p 360.

[3] Agrell J. & White R.A.; 1974, "An Experimental Investigation of Supersonic Axisymmetric Flow over Boattails Containing a Centered Propulsive Jet", FFA, TN AU-913.

[4] Herrin J.L. & Dutton C.J.; 1994, "Supersonic Near-wake Afterbody Boattailing Effects on Axisymmetric Bodies", J. Spacecrafts and Rockets, **31**, p 1021.

[5] Bowman J.E. & Clayden W.A.; 1967; "Cylindrical Afterbodies in Supersonic Flow with Gas Ejection", AIAA.J., **4**, p 1524.

[6] Sykes D.M.; 1970, "Cylindrical and Boattailed Afterbodies in Transonic Flows with Gas Ejection", AIAA.J., **8**, p 588.

[7] Andersson K., Gunners N.-E. & Hellgren R.; 1976, "Swedish Base Bleed – Increasing the Range of Artillery Projectiles through Base Flow", Propellants & Explosives, **1**, p 69.

[8] Gunners N.-E., Andersson K. & Hellgren R.; 1988, "Base-Bleed Systems for Gun Projectiles", Gun Propulsion Technology, Steifel L. (ed.), Progress in Astronautics & Aeronautics, **100**, p 27.

[9] Herrin J.L. & Dutton C.J.; 1994, "Supersonic Base Flow Experiments in the Near Wake of A Cylindrical Afterbody", AIAA.J., **32**, p 77.

[10] Mathur T. & Dutton J.C.; 1996, "Base-Bleed Experiments with a Cylindrical Afterbody in Supersonic Flow", J. Spacecrafts & Rockets, **33**, p 30.

[11] Bourdon C.J., Dutton J.C., Smith K.M. & Mathur T.; 1998, "Planar Visualisations of Large Scale Turbulent Structures in Axisymmetric Supersonic Base Flows", AIAA Paper No. 98- 0624.

[12] Delery J. & Lacau R.G.; 1987, "Prediction of Base Flows", AGARD Report 654.

[13] Launder, B.E. & Spalding, D.B., 1972, "Mathematical Models of Turbulence", Academic Press, London.

[14] Sagaut, P.: Large Eddy Simulation for Incompressible Flows, Springer Verlag, Heidelberg, 2001.

[15] Nikitin N.V., Nicoud F., Wasistho B., Squires K. D. & Spalart P.R.; 2000, "An Approach to Wall Modelling in Large Eddy Simulations", Phys. Fluids, **12**, p 1629.

[16] Reynolds W.C.; 1990, "The Potential and Limitations of Direct and Large Eddy Simulations" in Wither Turbulence? Turbulence at the Crossroads, ed. Lumley J.L., Lecture Notes in Physics, **357**, Springer Verlag, p 313.

[17] Putnam L.E. & Bissinger N.C.; 1985, "Results of AGARD Assessment of Prediction Capabilities for Nozzle Afterbody Flows", AIAA Paper 85-1464.

[18] Smagorinsky J.; 1963, "Numerical Study of Small Scale Intermittency in Three-dimensional Turbulence", Mon. Weather Rev., **91**, p 99.

[19] Kim W.-W. & Menon S.; 1997, "Application of the Localized Dynamic Subgrid Scale Model to Turbulent Wall-Bounded Flows", AIAA Paper No 97-0210.

[20] Kim W.-W., & Menon S.; 1999, "A new Incompressible Solver for Large-Eddy Simulations", Int. J. Num. Fluid Mech., **31**, p 983.

[21] Hirsch C.; 1999, "Numerical Computation of Internal and External Flows", J. Wiley & Sones.

[22] Fureby C. & Grinstein F.F.; 2002, "Large Eddy Simulation of High Reynolds-Number Free and Wall Bounded Flows", J. Comp. Phys., **181**, p 68.

[23] Grinstein F.F. & Fureby C.; 2002, "Recent Progress on MILES for High Re Flows", J. Fluids Engng., **124**, p 848.

[24] Jimenez J.; 1992, "Kinematic Alignment Effects in Turbulent Flows", Phys. Fluids, A **4**, p 652.

[25] Grinstein F.F. & DeVore C.R.; 1996, "Dynamics of Coherent Structures and Transition to Turbulence in Free Square Jets", Phys. Fluids, **8**, p 1237.

[26] Boris J.P. & Book D.L.; 1973, "Flux Corrected Transport I, SHASTA, a Fluid Transport Algorithm that Works", J. Comp. Phys. **11**, p 38.

[27] Grinstein F.F. & Karniadakis G.E.; 2002, "Special Section on Alternative LES and Hybrid RANS/LES for Turbulent Flows", J. Fluids Eng., **124**, p 821.

[28] Herrin J.L.; 1993, "An Experimental Investigation of Supersonic Axisymmetric Base Flow Including the Effects of Afterbody Boattailing", PhD Thesis, Univ. of Illinois at Urbana-Champaign, Urbana, IL.

[29] Poinsot T.J. & Lele S.K.; 1992, "Boundary Conditions for Direct Simulation of Compressible Viscous Reacting Flows", J. Comp. Phys., **101**, p 104.